

# PREDICTION OF PERMEABILITY USING OPTICAL COHERENCE TOMOGRAPHIC IMAGING OF AN EPOXY AND UNIDIRECTIONAL E-GLASS COMPOSITE

*Joy P. Dunkers, Frederick R. Phelan, Carl G. Zimba,  
Kathleen M. Flynn and Richard C. Peterson  
Polymers Division  
National Institute of Standards and Technology  
Gaithersburg, MD 20899*

*Rohit Prasankumar and James G. Fujimoto  
Department of Electrical Engineering  
Massachusetts Institute of Technology  
Cambridge, MA 02139*

## Abstract

Knowledge of the permeability tensor in liquid composite molding is important for process optimization. Unfortunately, experimental determination of the permeability is difficult and time consuming. A rapid, non-destructive technique called optical coherence tomography (OCT) can image the microstructure of a composite in minutes. In this work, binary images were generated from the OCT data and input into a lattice Boltzmann model for permeability prediction. Calculated permeabilities agreed well with experimental values for the same fiber volume fraction.

## Introduction

Fluid flow in Liquid Composite Molding (LCM) processes such as resin transfer molding (RTM) is usually modeled using Darcy's Law given by

$$\mathbf{v} = -\frac{\mathbf{K}}{\mu} \cdot \nabla P \quad (1)$$

where  $\mathbf{v}$  is the average (superficial) velocity in the medium,  $P$  is the pressure,  $\mathbf{K}$  is a symmetric, second order tensor known as the permeability and  $\mu$  is the fluid viscosity. Darcy's law is a volume-averaged model in which all the complicated interaction that takes place between the fluid and the fiber preform structure is accounted for through the permeability. Accurate permeability data, therefore, are a critical requirement if *a priori* modeling efforts based on Darcy's law are to be successfully used in the design and optimization of these processes. Currently, the most reliable and commonly used technique for obtaining permeability values is via experimental measurements in either radial or uni-directional flow configurations [1]. However, experimental characterization is slow, as it involves a large number of carefully controlled

experiments over a large range of volume fractions. Another more serious limitation is that it is difficult to conduct experiments on the materials in the deformed states they encounter when placed in LCM tooling, although there have been some recent efforts [2].

In light of these limitations, computational prediction of permeability [3-6] offers a potentially accurate and robust alternative to experimental methods. Such calculations involve imposing a pressure drop across the media, solving the appropriate transport equations for the detailed flow field, and then back-calculating the permeability by applying Darcy's law. The biggest drawback of this approach has been the inability to accurately determine the detailed geometry of the fibrous preform materials, which in addition to many intricate structural features, typically contain statistical variations and defects in their microstructure [7]. Without a precise representation of the media, it is not possible to accurately predict permeability values using computational methods.

There have been two main approaches to the problem of microstructure determination. The first is to perform calculations on small, computationally efficient "unit cell" structures using nominal dimensions that represent the average preform weave structure. The major problem with this approach is that calculations on the "average" unit cell structure do not in general, yield an accurate value for the average permeability [7]. A second approach is to determine the microstructure via optical methods (e.g., microscopy), and directly perform the numerical calculation on a discretization of the optical image. This approach has the advantage of exactly representing the media, and by including large sections of the media in the image, variations and defects in the microstructure are automatically accounted for in the calculation. However, until recently, this approach was probably even more tedious to perform than direct experimental measurement of permeability since the

composite specimens typically had to be carefully sectioned, polished and examined. However, a new technique being investigated in this work called optical coherence tomography (OCT) offers a means for rapidly and non-destructively determining the microstructure of fiber reinforced plastic materials, potentially leading to a robust means of computational permeability prediction.

Optical coherence tomography is a non-invasive, non-contact optical imaging technique that allows the visualization of microstructure within scattering media [8-10], OCT uses light in a manner analogous to the way ultrasound imaging uses sound, providing significantly higher spatial resolution (5 to 20  $\mu\text{m}$ ) albeit with shallower penetration depth. OCT is based upon low-coherence optical ranging techniques where the optical distance to individual sites within the sample is determined by the difference in time, relative to a reference light beam, for an incident light beam to penetrate and backscatter within the sample. This temporal delay is probed using a fiber optic interferometer and a broadband laser light source. The fiber optic interferometer consists of single-mode optical fiber coupled with a 50/50 fiber optic splitter that illuminates both the sample and a linearly translating reference mirror. Light reflected from the reference mirror recombines with light back-scattered and reflected from the sample at the 50/50 splitter to create a temporal interference pattern which is measured with a photodiode detector. The resulting interference patterns are present only when the optical path difference of the reference arm matches that of the sample arm to within the coherence length of the source. The axial, or y, spatial resolution that can be obtained with OCT is determined by the coherence length, or inverse spectral width, of the source and is typically 10 to 20  $\mu\text{m}$  (Figure 1). The source is typically a superluminescent diode laser, with a resolution as low as 7  $\mu\text{m}$ . The transverse, or x, spatial resolution of OCT is determined by the focal spot size on the sample which is typically 10 to 30  $\mu\text{m}$ . The ultimate limitation on the depth of penetration within the sample is the attenuation of light caused by scattering. Three-dimensional images of the sample are obtained by rastering the sample in x between successive OCT measurements along the z-axis.

In this work, OCT was used to image an epoxy/unidirectional E-glass composite. The volumetric images were converted to binary and input into a flow code for prediction of axial and transverse permeabilities. The predicted permeabilities of different image processing routines are compared with experimental values.

## Experimental

### Materials

The epoxy resin systems consisted of a diglycidyl ether of bisphenol A (DGEBA) monomer (Tactix123 , Dow Chemical Company, Midland, MI) and two amines [11]. Aromatic methylene dianiline (MDA) and aliphatic poly(propylene glycol)bis(2-aminopropyl ether) (JeffamineD400) ( $M_n \approx 400$ ) were purchased and used as received from Aldrich (Minneapolis, MN). The oxirane/amine stoichiometry was 2 mol oxirane/1 mol amine. The amine composition that consisted of 0.07 mol MDA and 0.93 mol D400. The refractive index of the postcured resin and of the fibers is  $1.552 \pm 0.004$  and  $1.554 \pm 0.004$ , respectively, as measured by white light and index matching fluids.\* The refractive index of the epoxy composites is calculated by the rule of mixtures for the resin and the fiber volume fraction:  $V_{resin}=0.56$ ,  $V_{fiber}=0.44$ ,  $(n_{resin})(V_{resin}) + (n_{fiber})(V_{fiber}) = n_{composite} = 1.55$ . The axial length or depth of field is:  $4.5 \text{ mm}/1.55=2.9 \text{ mm}$  for image. Details of the mixing and RTM are provided elsewhere [12].

### Instrumentation

The imaging system used in this study is schematically shown in Figure 1. A commercial superluminescent light source (AFC Technologies inc., Hull, Quebec, Canada) was used for the studies reported here. The source operated at 1.3  $\mu\text{m}$  with an output power of up to 15 mW and a spectral bandwidth of 40 nm, corresponding to an axial spatial resolution of  $\approx 20 \mu\text{m}$ . The laser light was coupled into a single-mode fiber-optic Michelson interferometer and delivered to both the reference mirror and the sample. The reference mirror was mounted on a rotating galvanometer, which is driven with a sawtooth voltage waveform. Transverse scanning was performed using a computer controlled motorized stage to translate the sample.

The interferometric signal was electronically filtered with a bandpass centered on the fringe or heterodyne frequency. The filtered fringe waveform is then demodulated, digitized and stored on a computer. The high dynamic range of this system allows back-reflections as weak as femtowatts of power to be detected. Images are displayed by mapping the logarithm of the signal strength to a gray scale look-up table. The acquisition time for each image was approximately 1 min. The axial (y) measurement range was determined by the distance the reference mirror moves (4.5 mm) normalized by the refractive index (n) of the sample:  $4.5 \text{ mm}/n$ . The probe beam was focused to a 30  $\mu\text{m}$  diameter spot at a depth of approximately 750  $\mu\text{m}$  to 1000  $\mu\text{m}$  below the surface of the sample.

---

\* The symbol  $\pm$  means plus or minus and is a standard measure of error.

## Image Processing

An automated image processing program was written using MATLAB 5.1 with the Image Processing Toolbox to convert the raw gray scale OCT images to binary images of glass fiber and epoxy (Figure 2). The raw image is first rotated and cropped to eliminate sample tilt and edge effects, yielding an image such as in Figure 2a, where the darker ellipses correspond to the three cross-sectional layers of fiber tows while the lighter regions are due to the epoxy. The image is then doubled in size by linear interpolation of adjacent pixels to minimize any artificial alteration of the tow size in subsequent image processing. To increase the contrast between the darker tows and the lighter epoxy regions, a variance image is created replacing the intensity value of a 2x2 cluster of pixels with the standard deviation of that cluster. In the next two steps, spurious light pixels within the tow regions and vertical lines corresponding to detector saturation are eliminated. Using the automated program, the boundary of the tows are determined and a binary image (Figure 2b) is formed. An additional operation may be performed to smooth the rough boundaries of the tows. The resulting binary image is then used as input for the permeability modeling.

## Numerical Simulation

### Governing Equations

Modeling of microscale flow in fibrous porous media is complicated by the existence of an open region around the tows, and a porous media inside the tows. Following previous studies [3-7], the Stokes equation, given by

$$\nabla P = \mu \nabla^2 v \quad (2)$$

is used to model flow in the open regions, and the Brinkman equation, given by

$$\nabla P = \mu \nabla^2 v - \underline{\underline{K}}^{-1} \cdot v \quad (3)$$

is used to model flow in the porous regions, where  $\underline{\underline{K}}$  is the permeability of the porous tows. In both regions, the continuity equation,

$$\nabla \cdot v = 0 \quad (4)$$

is used to model conservation of mass.

### Lattice Boltzmann Method

Solutions to the governing equations above are obtained using a lattice Boltzmann method previously described in detail elsewhere [5,6]. In short, the method involves the solution of the discrete Boltzmann equation for the particle velocity distribution function  $n_\alpha(x,t)$ , where traditional fluid flow quantities such as density and velocity are obtained through the moment sums

$$\rho = m \sum_{\alpha=1}^N n_\alpha(x,t) \quad (5)$$

$$u = \frac{m}{\rho(x,t)} \sum_{\alpha=1}^N v_\alpha n_\alpha(x,t) \quad (6)$$

where  $\rho(x,t)$  and  $u(x,t)$  are the macroscopic fluid density and velocity,  $m$  is the mass of fluid,  $v_\alpha$  are components of the discrete velocity space, and  $N$  is the number of velocities comprising the velocity space. The particle distribution function  $n_\alpha(x,t)$  is governed by the discrete Boltzmann equation given by

$$n_\alpha(x+v_\alpha, t+1) = n_\alpha(x,t) + \delta_\alpha(x,t) \quad (7)$$

where  $\delta_\alpha(x,t)$  is the collision operator which couples the set of velocity states  $v_\alpha$ . Most LB formulations employ the linear ‘‘BGK’’ form [5,6,13] of the collision operator in which the distribution function is expanded about its equilibrium value

$$\delta_\alpha(x,t) = -\frac{n_\alpha(x,t) - n_\alpha^{eq}(x,t)}{\tau} \quad (8)$$

where  $n_\alpha^{eq}(x,t)$  is called the equilibrium distribution function and  $\tau$  is a relaxation time for collisions controlling the rate of approach to equilibrium. The form of the equilibrium distribution function depends on the particular lattice model chosen. The three-dimensional, ‘‘d3q15’’ model [13] which resides on a cubic lattice is used here (d3 indicates the model is three-dimensional, q15 refers to the number of components in the velocity space). For this model, the equilibrium distribution function is given by

$$n_i = \frac{1}{9} \rho \left( 1 + 3 \frac{(e_i \cdot u)}{c} + \frac{9}{2} \frac{(e_i \cdot u)^2}{c^2} - \frac{3}{2} \frac{u^2}{c^2} \right), i=1,6 \quad (9)$$

$$n_i = \frac{1}{72} \rho \left( 1 + 3 \frac{(e_i \cdot u)}{c} + \frac{9}{2} \frac{(e_i \cdot u)^2}{c^2} - \frac{3}{2} \frac{u^2}{c^2} \right), i=7,14 \quad (10)$$

$$n_{15} = \frac{2}{9} \rho \left( 1 - \frac{3}{2} \frac{u^2}{c^2} \right) \quad (11)$$

where  $v_\alpha = c e_\alpha$ , and  $c$  is the lattice velocity.

### Permeability Computation

Permeability for different flow directions was computed by imposing a constant pressure along opposite faces of the lattice in the desired direction and integrating the system of equations above to steady-state. Estimates for the intra-tow permeability values were obtained from the formulas given in [3]. The steady-state velocity field at

the inlet was integrated over the surface to obtain the flow rate,  $Q$ , and this was used in the formula

$$K_{eff} = \frac{\mu QL}{A\Delta P} \quad (12)$$

to obtain the effective permeability,  $K_{eff}$ , for the desired direction.

## Results and Discussion

The results from the permeability calculation are shown in Table 1. The value for the experimental permeability is a result from one axial flow experiment, and the error associated with it is taken from previous work with this reinforcement [14]. Data sets within this table were processed in two different ways: For the “Manual” method, the tow outlines were drawn by sight and filled in. Images using the “Automated” method were processed as described above. For Data 2, the axial K of  $3.81 \times 10^{-4} \text{ mm}^2$  is considered to be the best possible value because the images are manually drawn. For the automatically processed images in Data 3, the axial K of  $2.83 \times 10^{-4} \text{ mm}^2$  is much lower than for Data 2. If the Brinkman fractions, or the fractional area occupied by the tows, are considered, then the axial K for Data 3 should be higher than for Data 2 since the Brinkman fraction for Data 3 is slightly lower than for Data 2. From these results and from analysis of the fluid velocity data, we conclude that the roughness of the border between the tows and the resin has a large influence on the magnitude of the flow. This influence propagates to the middle of the channels between the tows where fluid velocity should be at a maximum.

This conclusion is supported by results from Data 6 where a substantial drop in axial K resulted when compared to Data 2. These images are originally from Data 2 and were roughened to retain the nominally same Brinkman fraction. Additional evidence is provided in Data 7. The axial K from Data 7 is calculated from images in Data 2. The tows were dilated to increase the Brinkman fraction but not the tow roughness. When the axial K from Data 7 is compared to Data 6, the result is initially unexpected. A relative increase of roughly 4% of the Brinkman fraction in Data 7 should lead to a decrease in axial K over Data 6, but the result is the opposite. This comparison lends additional support to the idea that tow roughness, when Brinkman fractions are similar, has a substantial impact on the predicted permeability. These results also highlight the importance of processing the images as close to the actual structure as possible.

## Summary

The microstructure of a glass reinforced composite was accurately and rapidly obtained using

optical coherence tomography. OCT images were processed and input into a microscale flow model for permeability prediction. The axial and transverse permeabilities were predicted. The permeability values, while not within 20% error, were considered reasonably good. The results highlighted the importance of boundary roughness generated during image processing.

## Acknowledgements

This work was supported in part by a grant from the US Department of Commerce, contract 70NANB6H0092. We gratefully acknowledge technical contributions of Drs. Juergen Herrmann, Wolfgang Drexler, and Xingde Li.

## References

1. Parnas, R. and Salem, A. *Polymer Composites*, **14**(5), 383(1993).
2. Friedman, H., Johnson, R., Miller, B., Salem, D., and Parnas, R. *Polymer Composites*, **18**(5), 663(1997).
3. Ranganathan, S., Wise, G., Phelan Jr., F., Parnas, R., and Advani, S. *Advanced Composites X: Proceedings of the 10<sup>th</sup> Annual ASM/ESD Advanced Composites Conference and Exposition (ACCE94)*, ASM International, 309(1994).
4. Phelan Jr., F. and Wise, G. *Composites: Part A*, **27A**(1), 25 (1996).
5. Spaid, M. and Phelan Jr., F. *Phys. Fluids*, **9**(9), 2468 (1997).
6. Spaid, M. and Phelan Jr., F. *Composites: Part A*, **29**, 749, (1998).
7. Ranganathan, S., Easterling, R., Advani, S., and F. Phelan Jr., F. *Polymers & Polymer Composites*, **6**(2), 63, (1998).
8. Huang, D., Swanson, E., Lin, C., Schuman, J., Stinson, W., Chang, W., Hee, M., Flotte, T., Gregory, K., Puliafito, C., and Fujimoto, J.G. *Science*, **254**, 1178, (1991).
9. Fujimoto, J., Brezinski, M., Tearney, G. Boppart, S., Bouma, B., Hee, M., Southern, J. and Swanson, E., *Nature Medicine*, **1**, 970, (1995).
10. Bashkansky, M., Duncan, M., Kahn, M., Lewis, D., Reintjes, J., *Opt. Lett.*, **22**, 61(1997).
11. Identification of a commercial product is made only to facilitate experimental reproducibility and to adequately describe experimental procedure. In no case does it imply endorsement by NIST or imply that it is necessarily the best product for the experimental procedure.
12. Dunkers, J., Parnas, R., Zimba, C., Peterson, R., Flynn, K., Fujimoto, J., and Bouma, B. *Composites, Part A*, in press.
13. Hou, S., Lattice Boltzmann Method for Incompressible, Viscous Flow, Ph.D. Dissertation, Department of

Mechanical Engineering, Kansas State University,  
Manhattan, Kansas, (1995).

14. Parnas, R., Flynn, K. and Dal-Favero, M. *Polymer Composites*, **18(5)**, 623(1997).

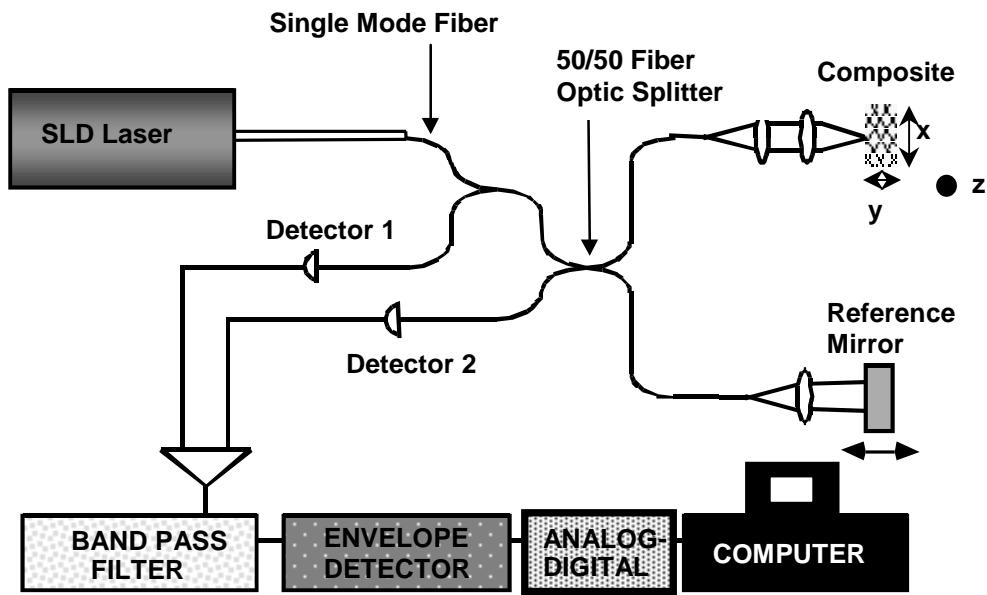


Figure 1: Schematic representation of the solid state laser and OCT system layout.

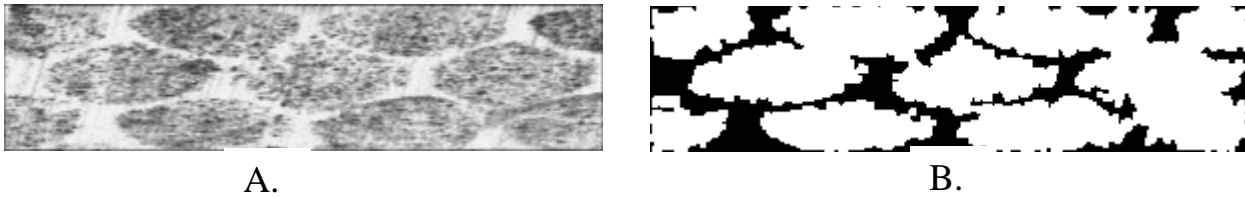


Figure 2: Original grayscale OCT image of the epoxy/ unidirectional E-glass composite. (A.), Binary OCT image after automated image processing (B.).

Sample Name	Type of Processing	Image Set	Axial K $\times 10^{-4}$ (mm <sup>2</sup> )	Transverse K $\times 10^{-4}$ (mm <sup>2</sup> )	Anisotropy Ratio	Brinkman Fraction
Experimental	-	-	$5.3 \pm 1.1$			0.770
Data 1	Manual	87-91	4.45	0.882	5.06	0.767
Data 2	Manual	75-95	3.81	0.992	4.11	$0.788 \pm 0.021$
Data 3	Automated No Smoothing	75-95	2.83	0.654	4.32	$0.768 \pm 0.021$
Data 4	Automated Smoothing	75-95	3.18	0.991	3.21	$0.750 \pm 0.027$
Data 5	Automated Smoothing	4-24	5.09	0.934	5.45	$0.727 \pm 0.014$
Data 6	Manual Roughened	75-95	2.73	0.662	4.12	$0.795 \pm 0.021$
Data 7	Manual Dilated	75-95	2.99	0.767	3.90	$0.837 \pm 0.020$

Table 1: Values of experimental and calculated permeabilities and corresponding Brinkman fractions.